Lab on a Chip

Cite this: *Lab Chip*, 2012, **12**, 4894–4902

www.rsc.org/loc

PAPER

Syngas generation from *n*-butane with an integrated MEMS assembly for gas processing in micro-solid oxide fuel cell systems

A. Bieberle-Hütter,*[a] A. J. Santis-Alvarez,[b] B. Jiang,[cd] P. Heeb,[e] T. Maeder,[d] M. Nabavi,[b] D. Poulikakos,[b] P. Niedermann,[f] A. Dommann,[f] P. Muralt,[c] A. Bernard[e] and L. J. Gauckler[a]

Received 16th July 2012, Accepted 7th September 2012
DOI: 10.1039/c2lc40809k

An integrated system of a microreformer and a carrier allowing for syngas generation from liquefied petroleum gas (LPG) for micro-SOFC application is discussed. The microreformer with an overall size of 12.7 mm × 12.7 mm × 1.9 mm is fabricated with micro-electro-mechanical system (MEMS) technologies. As a catalyst, a special foam-like material made from ceria-zirconia nanoparticles doped with rhodium is used to fill the reformer cavity of 58.5 mm^3. The microreformer is fixed onto a microfabricated structure with built-in fluidic channels and integrated heaters, the so-called functional carrier. It allows for thermal decoupling of the cold inlet gas and the hot fuel processing zone. Two methods for heating the microreformer are compared in this study: a) heating in an external furnace and b) heating with the two built-in heaters on the functional carrier. With both methods, high butane conversion rates of 74%–85% are obtained at around 550 °C. In addition, high hydrogen and carbon monoxide yields and selectivities are achieved. The results confirm those from classical lab reformers built without MEMS technology (N. Hotz *et al.*, *Chem. Eng. Sci.*, 2008, **63**, 5193; N. Hotz *et al.*, *Appl. Catal., B*, 2007, **73**, 336). The material combinations and processing techniques enable syngas production with the present MEMS based microreformer with high performance for temperatures up to 700 °C. The functional carrier is the basis for a new platform, which can integrate the micro-SOFC membranes and the gas processing unit as subsystem of an entire micro-SOFC system.

Introduction

Micro-solid oxide fuel cells (micro-SOFC) are miniaturized high temperature fuel cells with potential applications as battery chargers or battery replacement in mobile and portable devices.[3–6] Micro-SOFCs operate at much lower temperatures (350–550 °C) than conventional SOFCs (800–1000 °C) and are much smaller. A prominent design for micro-SOFC systems is the miniaturized tubular design which is based on microtubes either in the form of needles of 0.4 mm in diameter[7] or of flat tubes of 0.2 cm in thickness and 1.3 cm in width.[8] With the needle type design a power density of 80 mW cm^{-2} at 450 °C and of 300 mW cm^{-2} at 550 °C was achieved for single cells,[7] leading to a stack performance of 1.5 W at 500 °C for a 1 cm^3 stack at an OCV of 2.8 V.[9] The flat tubular design reached 100 mW cm^{-2} at 500 °C and 550 mW cm^{-2} at 700 °C.[8] Next to these tubular designs, planar designs processed with micro-electromechanical systems (MEMS) techniques are investigated by several groups worldwide.[10–16] These micro-SOFCs are based on thin film deposition and microfabrication with lithographic processes. Many studies have recently focused on the fabrication of single thin films and on their characterization for SOFC application, such as those reported in ref. 17–34. For the application, three thin films, *i.e.* the anode, the electrolyte and the cathode, are used and fabricated to a free-standing membrane. In this way, gas can be supplied to the reducing and oxidizing sides of the fuel cell. On Si substrates, power densities of 270 mW cm^{-2} at 350 °C[35] and 861 mW cm^{-2} at 450 °C for corrugated electrolyte membranes[13] were reported. On Foturan substrates, a power density of 152 mW cm^{-2} was obtained at 550 °C for an OCV of 1.06 V.[9] Diverse designs and approaches for micro-SOFC membranes are currently under investigation and are summarized in ref. 12. In addition to the tubular and the planar MEMS designs, ultra-thin ceramic foils made by ceramic technology were recently suggested for micro-SOFC applications.[36]

Besides the efforts on the investigation of SOFC thin film materials and the preparation of electrochemically active micro-SOFC membranes, reports about the development of an entire micro-SOFC system[3,6] are rare. In addition to the electrochemically

[a]*Nonmetallic Inorganic Materials, ETHZ, Zurich, Switzerland. E-mail: anja.bieberle@alumni.ethz.ch*
[b]*Laboratory of Thermodynamics in Emerging Technology, ETHZ, Zurich, Switzerland*
[c]*Ceramic Laboratory, EPFL, Lausanne, Switzerland*
[d]*Laboratory of Microengineering for Manufacturing, EPFL, Lausanne, Switzerland*
[e]*Institute for Micro- and Nanotechnology, NTB, Buchs, Switzerland*
[f]*Centre Suisse d'Electronique et de Microtechnique (CSEM), Neuchâtel, Switzerland*

active thin films, micro-SOFC systems include a gas processing unit, a thermal management system, and carrier elements such as electrical buffer, valves, ejectors, *etc.* The thermal characteristics of a micro-SOFC system, as well as the design requirements for a thermally self-sustaining operation of a micro-SOFC system, are discussed in detail.[37] It is found that the thermal design of a micro-SOFC system is strongly dependent on the size of the entire system. The gas processing unit consists of a reformer that converts the fuel into hydrogen (H_2) and other species, and a post-combustor that burns the fuel which was not used in the electrochemical cells. Although the gas processing unit is a central part of the system, it is mainly the basic chemistry and catalysis that have been studied in lab equipment and simulations so far.[1,2,38–43] The results showed that butane and propane–butane gas mixtures are feasible fuels for a micro-SOFC system. These gases are readily available and well accepted in everyday use, such as for lighters and camping gas cartridges. Recent studies on the reforming of butane in a disk shaped reactor reported on a rhodium/ceria-zirconia nanoparticle catalyst[40] that converts butane at temperatures as low as 550 °C with selectivities towards H_2 and carbon monoxide, CO, of up to 92% and 82%, respectively. The catalyst was tested to be stable for at least 40 h.[1] A similar catalyst can also be used in a secondary gas processing unit for the combustion of the non-equilibrium exhaust gas from a micro-SOFC.[44,45]

Besides the choice of an efficient catalyst, the gas processing units of a micro-SOFC system have to fulfil several requirements and therefore pose several challenges on the design and fabrication. First, the gas processing units have to operate at similar temperatures to the micro-SOFC membranes, while having a high and stable catalytic activity over long periods of time. The fuel cell gases, mainly H_2, CO and oxygen (O_2), are small-molecule and highly aggressive gases which pose special requirements towards the sealing of a gas processing unit. The carbon contained in the fuel gas can lead to carbon deposition and can thereby destroy the catalyst. The gas processing unit also has to be very small and compatible with the micro-fabrication techniques and the design of the micro-SOFC membranes. Bonding and processing sequences are also important aspects to consider. Finally, the gas processing unit has to be designed so that it can be integrated into a micro-SOFC system. A possible design was recently proposed by Santis-Alvarez *et al.*[43] together with a detailed catalytic characterization of a microreformer. A microheater platform with fluidic channels was developed by Jiang *et al.*[46] and allows for the testing of such a microreformer or of other miniaturized SOFC components.

In the literature, miniaturized gas reformers based on MEMS processing techniques are described for methanol,[47–49] ethanol,[50,51] and methane.[52–62] A good overview of microreactors is given in ref. 63. Several current designs and performances are summarized in ref. 47. Conversion rates are usually between 90–100% and the reformer operates at temperatures of around 180–250 °C, 600 °C, and 500–700 °C for methanol, ethanol, and methane, respectively. Only a few MEMS based gas processing components for butane conversion are discussed in the literature.[64,65] In, ref. 64, a MEMS fuel processor is described consisting of suspended silicon nitride tubes comprising two independent U-shaped fluid channels. The tubes are fixed on one end into a silicon substrate while the channels are floating on the other end. The reactor can operate at up to 900 °C and a conversion rate of butane of 92.4% was observed during auto-thermal combustion of butane.

In ref. 65, several elements required for a gas processing unit are described. A catalytic micro-butane combustor is investigated which can be fabricated with MEMS techniques, such as deep reactive ion etching (DRIE), from a silicon base plate and a Pyrex top plate. The combustion chamber is 14 mm × 8 mm × 0.15 mm in size. Pt loaded TiO_2 catalyst is used and butane and air gases are applied. Stable combustion at power larger than 5 W is found. Butane is completely combusted and no unburned fragments, such as CO and hydrocarbons, are detected. The second component for gas processing discussed in this study is a combustor-integrated microfuel reformer. The steam reforming of methanol is demonstrated in this study using a SiO_2 membrane. The system could also be used for liquid fuel, such as butane; however, this was not shown in the study.

The literature overview shows that progress in miniaturized gas processing components was achieved in recent years. However, information about microreformers which could be directly coupled to micro-SOFC membranes and can operate at high temperature is sparse. We report therefore about an assembly of a microreformer and a functional carrier which allows for testing of the reformer on the carrier using either the integrated heaters and or an external furnace. This allows for direct comparison of microreformer fabricated with and without MEMS techniques, as well as performance testing of the functional carrier. The microreformer – functional carrier – assembly demonstrates a platform for subunit integration for micro-SOFC systems and its technical realization and testing is therefore an important step towards the development of micro-SOFC systems.

General design of microreformer and functional carrier

The general design of the microreformer and functional carrier assembly is shown in Fig. 1. The figure summarizes the processing, materials and components. Four main components can be identified: the microreformer, the functional carrier, the gas connectors, and the ceramic interconnector. The microreformer and the functional carrier are described in the following section. More detailed information can be obtained from ref. 43 and 46. The ceramic interconnector is made of a piece of alumina plate (Haldemann & Porret SA) with screen-printed thick-film electrical tracks (ESL 590G) and electrical pads (DuPont 6143). The dimension of the ceramic interconnector is 12.7 mm × 24.5 mm × 1.0 mm. The gas connectors are Ferro gas fittings; they are sealed onto the carrier with epoxy glue (STYCAST 2741W1).

Experimental

Fabrication of microreformer

The microreformer consisted of a MEMS structure which was filled with catalyst material.

Processing of the MEMS structure. The MEMS structure consisted of a borosilicate glass wafer (Borofloat 33) and a silicon wafer. Two holes of 2.0 mm in diameter were drilled in the

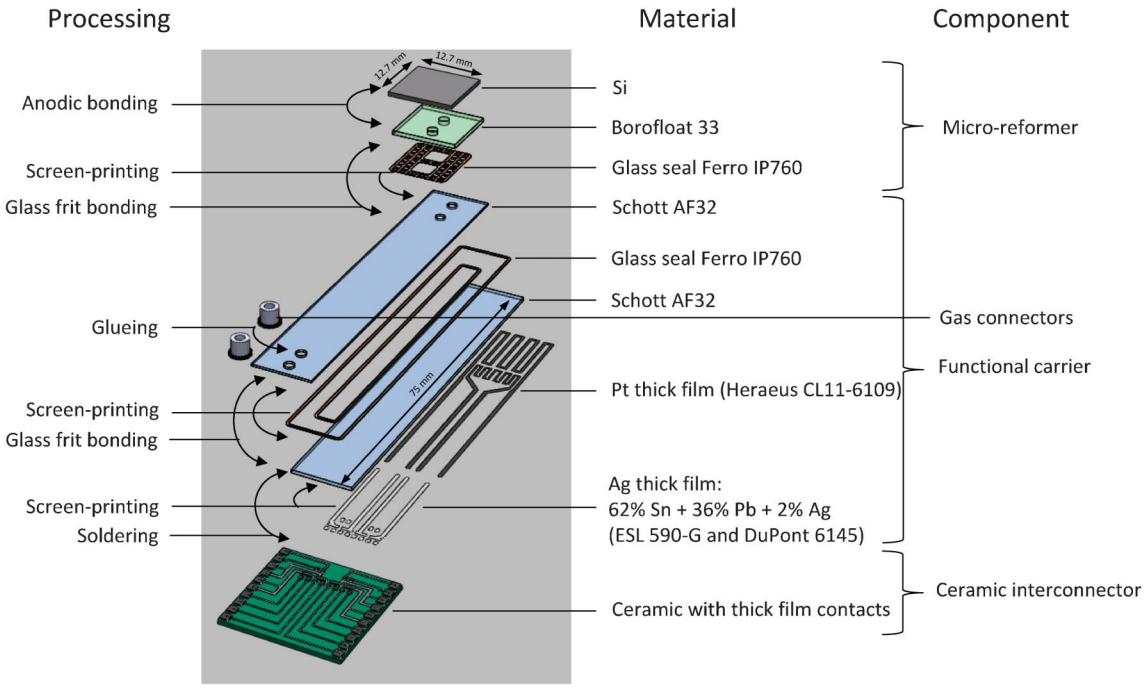

Fig. 1 Schematic of the microreformer – functional carrier – assembly.

Borofloat 33 wafer by ultrasonic drilling (performed at Dama Technologies AG, Switzerland) for gas inlet and outlet. For the catalyst cavity, a thermally oxidized silicon dioxide layer with 3 μm thickness was pre-structured by means of photolithography on the 1.0 mm thick silicon wafer. The pattern contained two mesas in the middle of the structure with 1.5 mm × 1.5 mm in size in order to add mechanical strength. Etching of the cavity was carried out with a 40% potassium hydroxide solution at 60 °C. Before bonding, both wafers were cleaned in buffered hydrofluoric etch (BHF) (1 BHF : 10 H_2O) for 64 min. Then, the patterned silicon wafer was joined to the Borofloat 33 wafer by anodic bonding in an EVG 520 bonding system at 425 °C and 400 V. The final dimensions of the catalyst cavity were 11.5 mm × 11.0 mm with a depth of 530 μm ± 3 μm. The total volume of the cavity was 58.5 mm^3. The anodically bonded wafers were finally sawed to a size of 12.7 mm × 12.7 mm.

Fabrication of catalytic material and filling into MEMS structure. Ceria-Zirconia ($Ce_{0.5}Zr_{0.5}O_2$) catalytic nanoparticles with 1.9 wt % rhodium-doping and an average size of 12 nm were synthesized by flame spray pyrolysis as described in ref. 2 and 66. A ceramic foam was prepared according to ref. 38 using 12.1 wt.% catalytic nanoparticles, 36.1 wt.% calcined SiO_2-sand (Riedel-deHaën, average diameter: 200 μm, puriss p.a.), 0.45 wt.% gelation agent (triammonium citrate, Riedel-deHaën, purity ⩾97%), 1.4 wt.% ceramic binder (sodium metasilicate pentahydrate, Riedel-deHaën, purity ⩾97%), and 50 wt.% of distilled water (R = 18 MΩ). The heterogeneous mixture was manually stirred and placed in an ultrasonic bath for 5 min. The paste-like mixture was slowly inserted into the reactor with the help of a spatula. In a final step, the water in the reactor was evaporated by thermal treatment using a heating rate of 2.5 °C min^{-1} and a final temperature of 100 °C for 60 min. Before assembly of the reformer onto the carrier structure, the reformer was heated to 650 °C for 20 min with a heating rate of 10 °C min^{-1}. This step was used in order to ensure that the catalytic bed could sustain such high temperatures without any crack formation.

Fabrication of functional carrier

The functional carrier was assembled from two pieces of aluminosilicate glass (Schott AF 32® Eco Glass) which has an average thermal expansion coefficient of 3.2 ppm/K up to 300 °C, close to the ones of silicon and Borofloat 33. The AF 32® Eco offers a higher thermal stability than the Borofloat 33, its glass transformation temperature is 715 °C compared to Borofloat 33 with 525 °C. The carrier was 12 mm × 75 mm in size and provided fluidic and mechanical interconnects to the microreformer. The top plate of the carrier was 0.5 mm thick and the bottom plate was 1.1 mm thick. The gas channels were applied by screen-printing of glass frit (Ferro IP760c) which also bonded the two aluminosilicate wafers together. The symmetric fluidic pattern defined a split inlet channel at the sides and an outlet channel at the center. Five layers of screen-printed sealing glass were applied to both the top and the bottom carrier plates. The plates were assembled and sintered at a peak temperature of 725 °C for 20 min with a weight of 80 g. The thickness of the sintered sealing glass layer was 0.15 mm ± 0.01 mm after processing.

For the heaters, thick film platinum (Pt, Heraeus CL11-6109) was screen-printed at the back of the carrier and fired at a peak temperature of 850 °C for 10 min. The thickness of the fired Pt metallization is 11.0 μm ± 2.0 μm. As a final step, thick-film silver (Ag) conductor (Electroscience ESL 590-G and DuPont 6145) was screen-printed onto the bottom carrier plate for connecting the Pt heater to the ceramic base. The Ag conductor was fired at 500 °C for 20 min. The gas tightness of the sealing

was evaluated by means of the dye penetrating method using an orange food colorant as dye (Allura Red AC).

Measurement set-up

The microreformer which was integrated onto the functional carrier was tested with two different methods with respect to heating. In the first method, the assembly was placed halfway in an external furnace with the microreformer side inside the furnace. In the second method, the microreformer was tested stand-alone, *i.e.* directly on the functional carrier with the built-in heaters.

Characterization in external furnace. For the characterization of the microreformer in the external furnace, the microreformer on the carrier was connected to the testing setup as described in detail in ref. 2 and 38. A stainless steel and a glass tube connection were used for the inlet and the outlet gases, respectively (Fig. 2). The mechanical interconnects were made by using a stainless steel connection and a glass tube, for inlet and outlet gases, respectively, and by sealing them using a silicone sealant (DOW CORNING®732, Dow Corning GmbH) able to keep its elasticity to up to 205 °C.

The microreformer on the carrier was placed inside the furnace so that the entire microreformer was heated to the set temperature, T_{set}. No insulation around the microreformer was added for this testing method. The set temperature was monitored by using a K-type thermocouple placed at the center of the silicon surface on the back of the microreformer. The partial oxidation catalyzed by the rhodium-nanoparticles in the microreformer was tested at T_{set} = 550 °C.

Characterization with integrated heaters. The measurement set-up is shown in Fig. 3. The inlet gas comes through the gas tubing (1) directly into the functional carrier (4). The microreformer (5) was fixed onto the functional carrier through a layer of glass frit (Ferro IP760c) and was fired at 675 °C for 20 min. The carrier was solder-attached (EFD, Sn62/Pb36/Ag2) onto the ceramic interconnector (3) at 210 °C for 30 s. The cantilever shape of the carrier offered thermal decoupling between the "hot" end of the carrier and the "cold" end. The printed circuit board (PCB) (2) was connected to the ceramic base through spring contacts providing constant voltage to the self-heating thermistor on the carrier structure. An aluminum mechanical base offered the overall mechanical carrier (6). Two pieces of thermal blocks (WDS© Ultra, Porextherm Daemmstoffe GmbH, coefficient of thermal conductivity at 500 °C: 0.027 W/(mK); size: 5 cm × 10 cm × 10 cm each) covered the mechanical base as thermal insulation (not seen in Fig. 2). The PCB, the mechanical base, and the thermal blocks allowed for characterization of the microreformer in standalone operation without a furnace. The heating capability and thermal decoupling of the functional carrier were characterized by a standard Pt1000 thermistor with a voltage supply that could be ramped up to 22 V. Different voltages were applied to the heaters at the bottom of the functional carrier. The corresponding current through the heaters were measured, which allowed calculation of the power consumption. At the same time, the obtained temperature at the top of the carrier and the temperature at the other end, the fluidic connection, were measured by using two Pt1000 thermistors.

Fig. 2 Measurement set-up for microreformer characterization in external furnace. Gas inlet is outside the furnace in the cold part of the carrier.

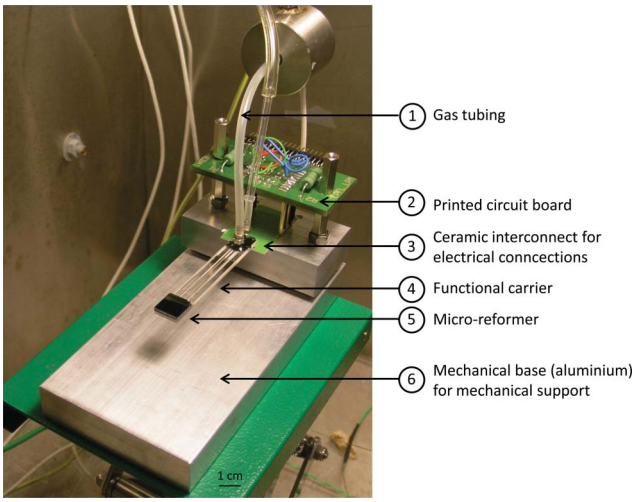

Fig. 3 Measurement set-up for microreformer characterization with integrated heaters: 1) gas tubing, 2) printed circuit board, 3) ceramic interconnector for electrical connections, 4) functional carrier in size of 12 mm × 75 mm, 5) microreformer, 6) mechanical base (aluminum) for mechanical support. Not seen between microreformer and mechanical base: WDS thermal blocks for thermal insulation.

Catalytic characterization of the microreformer

N-butane and synthetic air were mixed at room temperature at a carbon to oxygen (C/O) ratio of ϕ = 0.8 (eqn (1)) before the reactor inlet. This C/O ratio has already shown good results on the partial oxidation performance for *n*-butane for the same Rh-nanoparticles.[1,40,45] The total inlet flow rate was 30 standard cubic centiliters per minute (sccm).

$$\phi = 2 \cdot \frac{\dot{n}_{C_4H_{10},in}}{\dot{n}_{O_2,in}} \quad (1)$$

For both testing methods, a temperature was first targeted at the back of the microreactor when no gases were flowing through it

(T_{set}). Once T_{set} is obtained, the reacting gas mixture was purged into the testing platform and a temperature increase was obtained. This increase in temperature was caused by the exothermic catalytic oxidation reaction and was measured by a thermocouple placed at the center of the microreformer. This temperature was termed the operation temperature, T_{op}.

The conversion rate of butane, η, (eqn (2)) the yields, ψ, (eqn (3)) and the selectivities, S, (eqn (4)) of H_2, and CO, respectively, were determined as the characteristic values for the gas analysis. They were defined according to ref. 2 as follows:

$$\eta = \frac{\dot{n}_{C_4H_{10},in} - \dot{n}_{C_4H_{10},out}}{\dot{n}_{C_4H_{10},in}}, \quad (2)$$

$$\psi_{H_2} = \frac{\dot{n}_{H_2,out}}{5\dot{n}_{C_4H_{10},in}}$$
$$\psi_{CO} = \frac{\dot{n}_{CO,out}}{4\dot{n}_{C_4H_{10},in}} \quad (3)$$

$$S_{H_2} = \frac{\dot{n}_{H_2,out}}{\dot{n}_{H_2,out} + \dot{n}_{H_2O,out}}$$
$$S_{CO} = \frac{\dot{n}_{CO,out}}{\dot{n}_{CO,out} + \dot{n}_{H_2O,out}} \quad (4)$$

where $\dot{n}_x$ are the molar flow rates (mol s^{-1}) of the gas species X, *i.e.* C_4H_{10}, H_2, and CO. In and out signify inlet and outlet flow conditions, respectively. The standard deviation was derived from two measurements at the same operation point: the first measurement was done after about 90 min and the second after about 115 min of reaction time.

The gas compositions were monitored for both measurement methods by an online automated gas chromatograph (6890 GC) using a HP-PlotQ column.

Results and discussion

Fabrication of microreformer

Images of the microreformer before and after filling of the catalyst are shown in Fig. 4. The entire reformer weighs 662 mg whereas 78 mg is the weight of the reactor bed only. The two openings in the transparent Borofloat 33 wafer are for the connections of the gas inlet and outlet. The dark squares in the middle of the wafers are the mesas in the Si wafer which increase the mechanical stability of the bonded MEMS structure. The dark border in Fig. 4a indicates a good bonding of the silicon wafer to the Borofloat 33 wafer. The bonding is very reproducible and a yield of about 99% is obtained. The catalyst is filled very homogeneously into the cavity (Fig. 4b). After thermal treatment, no dead volume is visible in the microreformer.

The advantages of such a microreformer compared to a reformer which is not processed by MEMS techniques are the enhanced heat transfer due to the larger surface to volume ratio when reducing the dimensions, and the reduced viscous loss due to a lower Reynolds number. Besides, a higher dynamic response can be expected when reducing the reactor volume and its heat capacitance. Further, direct coupling to SOFC membranes is possible with this design.

Fabrication of functional carrier

A photo of the functional carrier with integrated microreformer (dark grey) and ceramic interconnector (light green) is shown in Fig. 5. Pt and Ag tracks are seen on the transparent carrier plates. Also the glass frit used for the gas channels as well as for the sealing is seen through the transparent AF 32® Eco glass. The process temperature for the glass seal depends on the viscosity of the glass frit. The maximum process temperature for this sealing glass on the carrier was found to be 725 °C. No cracks and deformations of the carrier are found. With large weight, the pressure applied on the carrier accelerated the mass flow of glass frit, filling the open space, but easily deforms or cracks the carrier itself. It is found that 80 g weight is the maximum weight that can be applied onto the carrier. The narrow width of the sealing glass layer brings less contact area of sealing layer from both carrier plates but increases the difficulty of building up the thickness of the fluidic channels. The width of the sealing glass layer is optimized to 0.5 mm. No degradation of the anodic bonding of the microreformer is observed after this process. Dye penetrating test experiments confirm good gas tightness.[46]

Thick-film Pt is used as the heating element on the carrier due to its good high temperature stability and linear temperature resistance coefficient below 600 °C.[67] As shown in Fig. 5, two

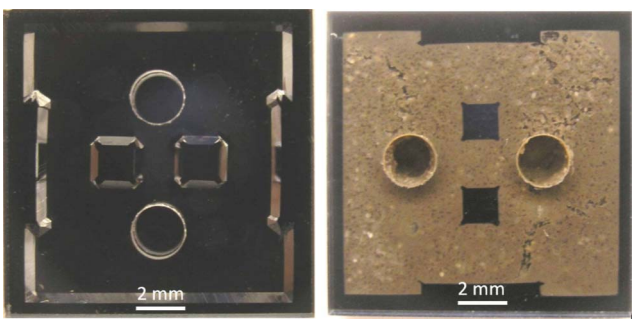

Fig. 4 Microreformer with two holes for gas inlet and outlet and two mesas for mechanical support: a) before filling of catalyst, b) after filling of catalyst and after thermal treatment.

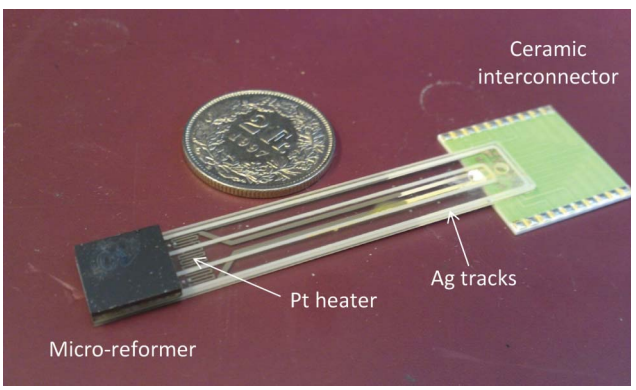

Fig. 5 Photo of the functional carrier with integrated microreformer and ceramic interconnector.

separated conduction tracks of thick-film Pt are fabricated at the bottom of the functional carrier, with the bigger one covering the major area underneath the "hot" end and the small one placed at the side of incoming gas mixture. This design aims to compensate the thermal loss from the cold gas feed in order to achieve homogenous heating throughout the entire microreformer. Thick-film Ag tracks are used in areas where the temperature is always below 300 °C; thus the overall resistance of the heating elements can be reduced and parasitic heating of the cold zone is largely avoided. The thick-film Ag also has good solderability with commercial solder products for attaching onto the ceramic interconnect. Thus, thick-film Ag is screen-printed at the back of the carrier and sintered at 500 °C for 10 min to connect the thick-film Pt and for the solder-attachment onto the ceramic interconnect. After fabrication, the resistance of the thick-film heater is 22 Ω.[46]

The thermal profile of the functional carrier in dependence of the consumed power is investigated for the two ends of the carrier, *i.e.* the hot zone and the cold zone (Fig. 6). It is seen that the temperature stays below 40 °C in the cold zone of the functional carrier for all powers. This is the case for the whole measurement period (>5 h). In the hot zone, the temperature increases parabolically from room temperature up to 700 °C with increasing power from 0 W to 4.8 W. Hence, temperatures up to 700 °C can be obtained with this measurement set-up. Thermal decoupling of the cold and hot zones is well achieved. The thermal capability of the functional carrier meets the temperature requirement of the microreformer and its characterization.

Catalytic characterization of the microreformer

The microreformer is tested and characterized with respect to its catalytic performance. The heating of the reformer is achieved by two methods: a) heating in an external furnace, b) heating using the integrated heaters of the functional carrier.

Characterization of the microreformer with heating in the furnace. The microreformer is integrated on the functional carrier. The heating is applied from an external furnace. The temperature at the middle of the reformer is first set to T_{set} = 550 °C. By applying the reformer gas with a total volumetric flow of 30 sccm, the temperature increases by 15 °C to an operating temperature of T_{op} = 565 °C. This temperature increase is due to exothermic reactions of the fuel gas. T_{op} can be considered as the average temperature on the entire microreformer and is high enough not only for high syngas generation from *n*-butane, but also for high electrochemical performance of SOFC membranes.[2,3,68]

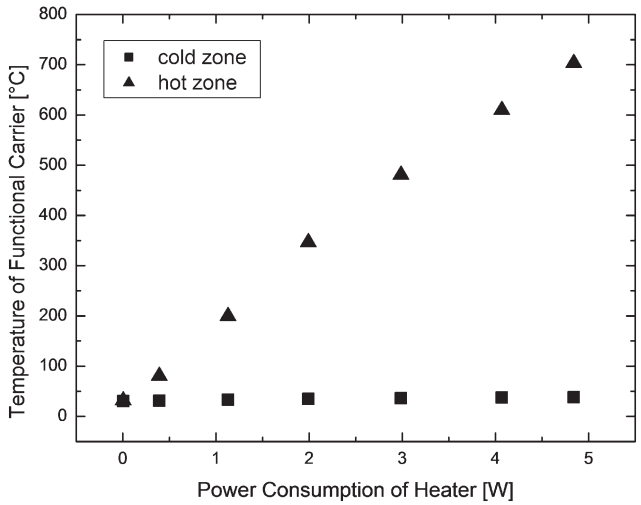

Fig. 6 Temperature profiles of the cold and hot zones of the functional carrier with characterization with integrated heaters.

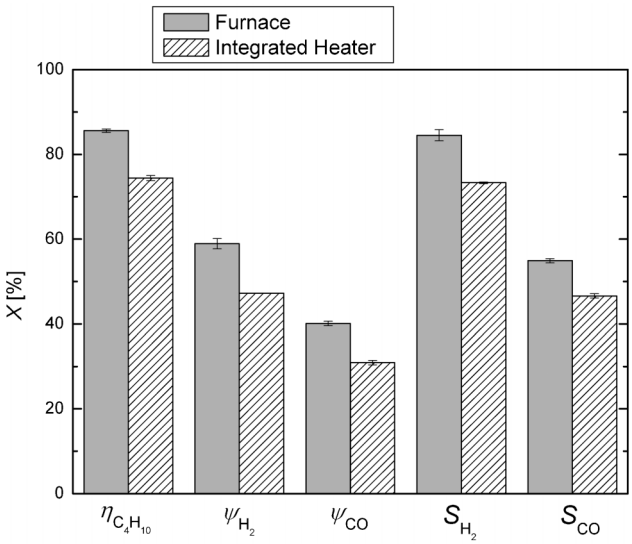

Fig. 7 Characteristic values from the gas analysis results of both testing modes at steady state. Testing in the furnace: T_{set} = 550 °C, T_{op} = 565 °C, volumetric flow = 30 sscm; testing on the functional carrier with integrated heaters: T_{set} = 350 °C, T_{op} = 560 °C.

Table 1 Outlet gas composition. Slight deviation from 100% results from averaging. The standard deviations are determined from two measurements under the same conditions, but different dwell times

Gas component	Furnace/vol (%)	Integrated heaters/vol (%)
N_2	58.9 ± 0.2	60.9 ± 1.2
H_2	17.4 ± 0.3	14.4 ± 0.3
CO	9.5 ± 0.1	7.5 ± 0.3
CO_2	7.8 ± 0.1	8.6 ± 0.1
H_2O	3.2 ± 0.3	5.2 ± 0.2
CH_4	1.4 ± 0.0	0.8 ± 0.0
C_4H_{10}	0.9 ± 0.0	1.6 ± 0.0
other C-species	0.0	0.0
O_2	0.0	0.0

The composition of the outlet gas of the microreformer is listed in Table 1 together with the volume percentage at the reactor outlet. The largest component in the outlet gas is inert nitrogen, N_2, with almost 59 vol%. It derives from the air used during the combustion process. Then, H_2, with 17.4 vol%, CO, with 9.5 vol%, and carbon dioxide, CO_2, with 7.8 vol% follow. Small amounts of water, H_2O, (3.2 vol%) and methane, CH_4, (1.4 vol%) are detected. The very small amount of butane, C_4H_{10} (<1%) indicates high fuel utilization for the partial oxidation reaction. No other hydrocarbons, such as C_3H_8 or C_2H_6, are found in the outlet gas. All oxygen, O_2, is fully converted as well. The standard deviations are determined from two measurements

Table 2 Characteristic values from the gas analysis results of both testing modes at steady state. Testing in the furnace: T_{set} = 550 °C, T_{op} = 565 °C, volumetric flow = 30 sscm; testing on the functional carrier with integrated heaters: T_{set} = 350 °C, T_{op} = 560 °C. The standard deviations are determined from two measurements under same conditions, but different dwell times

Heat source	$\eta_{C_4H_{10}}$/%	ψ_{H_2}/%	ψ_{CO}/%	S_{H_2}/%	S_{CO}/%
Furnace	85.6 ± 0.4	58.9 ± 1.2	40.1 ± 0.5	84.5 ± 1.3	54.9 ± 0.5
Integrated heaters	74.4 ±0.6	47.2 ± 0.0	30.9 ± 0.5	73.3 ± 0.2	46.6 ± 0.5

under same conditions, but different dwell times. The low standard deviations indicate that the process is very stable.

The catalytic results of the butane conversion in the reformer when measured in the furnace are shown in Table 2 and Fig. 7. It is found that 1.9 wt% $Rh/Ce_{0.5}Zr_{0.5}O_2$ catalytic nanoparticles are able to deliver butane conversion, $\eta_{C_4H_{10}}$, of 85.6% and a hydrogen yield, ψ_{H_2}, of 58.9%. Also, hydrogen selectivity, S_{H_2}, of 84.5% is measured, confirming the high selectivity for H_2 molecules towards H_2 production on the catalytic nanoparticle surface. For the second partial oxidation product carbon monoxide, a yield, ψ_{CO}, of 40.1% and selectivity, S_{CO}, of 54.9% are obtained.

Characterization of the microreformer with heating with the integrated heaters of the functional carrier. Power is first supplied to the integrated heaters on the functional carrier to achieve a temperature of T_{set} = 350 °C. This temperature is achieved in about 5–7 min and is sufficient to activate the catalytic reaction. After introduction of the reaction gases into the testing platform, a large temperature increase is obtained confirming the successful activation of reaction at this low starting temperature, T_{set}. About 95% of the operating temperature is obtained in less than 15 min. This is fast considering that the carrier was not optimized for fast heat-up as it was made of glass. After approximately 90 min reaction time, the reaction reached steady state conditions with an operating temperature of T_{op} = 560 °C. The product gas is listed in Table 1.

As shown in Table 2 and Fig. 7, a butane conversion, $\eta_{C_4H_{10}}$, of 74.4% is obtained. This lower *n*-butane conversion compared to the results in the furnace has a direct influence on the catalytic reaction *i.e.* on the production of hydrogen and carbon monoxide. The hydrogen and carbon monoxide yield are 47.2% and 30.9%, respectively. The hydrogen and carbon monoxide selectivities are 73.3% and 46.6%, respectively.

Discussion of the catalytic conversion results. The same outlet gases are found for both testing methods (Table 1). Also the percentages of the specific gases are in general very similar. A slightly better yield in H_2 and CO is found for the system with furnace heating. Also, higher performances in butane conversion rates, yields and selectivities are found for the system with furnace heating compared to that using the integrated heaters (Table 2, Fig. 7). One of the reasons for this is related to the thermal distribution and the insulation. In the case of the measurements in the furnace, the microreformer is not insulated and it is heated up homogeneously inside the furnace, providing quasi-isothermal conditions inside the catalytic bed. The temperature increase due to the exothermic reaction is 15 °C. In the case of the measurements on the integrated heaters, the microreformer is insulated with WDS thermal blocks and the heating is provided only from the bottom, therefore affecting areas where endothermic reactions take place.[1,40] The temperature rise provided by the oxidative reaction is 210 °C and leads to T_{op} of 565 °C. Due to these differences in the heating and insulation combined with the knowledge that the catalytic reaction is strongly dependent on the temperature, it becomes clear that shifts in performance are seen between the two different measurement set-ups. In order to increase the performance of the microreactor when measured with the integrated heaters, the entire chain of reactions has to be considered.

The difference in catalytic performance between both testing methods is also reflected in the total amount of molar flow rate of syngas products, which accounted for 6.9 μmol s^{-1} and 5.4 μmol s^{-1}, for the testing in the furnace and the testing with the integrated heaters, respectively. The relative difference in syngas molar flow rate amounts to 22% and is due to differences in the temperatures and the temperature distributions with the two methods.

In general, high performances are obtained with the microreformer with both measurement methods. The values are very close to the data measured in earlier studies with the same catalyst and similar temperatures, but with traditional disk shape or tubular reactor types, *i.e.* macroreformers.[1,2,38,43] The slightly lower performances with the microreactor discussed here are related to the very different testing set-up which influences space time,[2,69] heating of the inlet gases, and with it the overall reaction mechanism. Hence, it can be concluded that a microreformer with high conversion rate and syngas yield can be achieved for this temperature range. The results also show that a system with integrated heaters is possible and, hence, an integrated microsystem can be built for syngas production that can, for example, be coupled to a micro-SOFC system.

Summary and conclusion

An integrated system of a microreformer and a functional carrier is discussed in this study. The MEMS fabricated microreformer can convert LPG such as *n*-butane into syngas which can be used as feed for the electrochemical cells in a micro-SOFC system. The functional carrier allows for thermal decoupling of the cold inlet and the hot process gases as well as for direct heating of the microreformer in a complete system.

The microreformer integrated on the functional carrier was tested with two methods, *i.e.* in an external furnace and with the integrated heaters on the carrier. This allows for direct comparison of the MEMS fabricated microreformer to reformer fabricated without MEMS technology and at the same time for performance tests of the functional carrier. Butane conversion rates between 74% and 85%, hydrogen and carbon monoxide yield between 59% and 47%, and selectivities between 45% and 85 are obtained for testing in the furnace and with the integrated heaters, respectively, at temperatures of 550 °C and 565 °C. This performance is similar to the performance of reformers built

without MEMS technology and therefore proves unambiguously the possible application of this microreformer and functional carrier assembly as a gas processing unit in a micro-SOFC system. The results pave the way towards direct integration of a gas processing unit with SOFC membranes and close the gap regarding fuel supply within a micro-SOFC system. No significant differences between the two testing methods are found which proves that a system with integrated heaters allows for efficient syngas production at temperatures up to 700 °C.

The study shows a gas processing unit with small dimensions and based on simple MEMS fabrication techniques which can be integrated into a microsystem for temperatures up to 700 °C. The functional carrier is a self-standing miniaturized system which might serve in the future as a platform for an integrated gas processing and fuel cell membrane assembly for micro-SOFC application. The feasibility of this small sized and easy to fabricate system is shown. The compactness of the assembly makes it suitable for implementation in small portable power devices.

Acknowledgements

D. Bischof from the Interstaatliche Hochschule für Technik Buchs, Switzerland (NTB) is thanked for his effort in processing the microreformers. The ONEBAT consortium and the SOFC group at Nonmetallic Inorganic Materials at ETH Zurich, Switzerland, are thanked for collaboration and continuous discussion. Financial support from the Swiss National Science Foundation (SNSF) within the framework of the SINERGIA project "ONEBAT" (CRSI11_126830) is gratefully acknowledged. One of the authors (LJG) gratefully acknowledges the support of the International Institute for Carbon Neutral Energy Research (WPI-I2CNER), sponsored by the Japanese Ministry of Education, Culture, Sports, Science and Technology.

References

1 N. Hotz, N. Osterwalder, W. J. Stark, N. R. Bieri and D. Poulikakos, *Chem. Eng. Sci.*, 2008, **63**, 5193–5101.
2 N. Hotz, M. J. Stutz, S. Loher, W. J. Stark and D. Poulikakos, *Appl. Catal., B*, 2007, **73**, 336–344.
3 A. Bieberle-Hütter, D. Beckel, A. Infortuna, U. P. Muecke, J. L. M. Rupp, L. J. Gauckler, S. Rey-Mermet, P. Muralt, N. R. Bieri, N. Hotz, M. J. Stutz, D. Poulikakos, P. Heeb, P. Müller, A. Bernard, R. Gmür and T. Hocker, *J. Power Sources*, 2008, **177**, 123–130.
4 G. A. Tompsett, C. Finnerty, K. Kendall, T. Alston and N. M. Sammes, *J. Power Sources*, 2000, **86**, 376–382.
5 S. Suzuki, H. Uchida and M. Watanabe, *Solid State Ionics*, 2006, **177**, 359–365.
6 D. Nikbin, *The Fuel Cell Research*, 2006, **3**, 21–24.
7 T. Suzuki, Y. Funahashi, Z. Hasan, T. Yamaguchi, Y. Fujishiro and M. Awano, *Electrochem. Commun.*, 2008, **10**, 1563–1566.
8 T. Suzuki, B. Liang, T. Yamaguchi, K. Hamamoto and Y. Fujishiro, *Electrochem. Commun.*, 2011, **13**, 719–722.
9 T. Suzuki, Y. Funahashi, T. Yamaguchi, Y. Fujishiro and M. Awano, *Fuel Cells*, 2008, **8**(6), 381–384.
10 I. Garbayo, A. Tarancon, J. Santiso, F. Peiro, E. Alarcon-Lado, A. Cavallaro, I. Garcia, C. Cane and N. Sabate, *Solid State Ionics*, 2010, **181**, 322–331.
11 A. Tarancon, N. Sabate, A. Cavallaro, I. Gracia, j. Roqueta, I. Garbayo, J. P. Esquivel, G. Garcia, C. Cane and J. Santiso, *J. Nanosci. Nanotechnol.*, 2010, **10**, 1327–1337.
12 A. Evans, A. Bieberle-Hütter, J. L. M. Rupp and L. J. Gauckler, *J. Power Sources*, 2009, **194**, 119–129.
13 P. Su, C. Chao, J. Shim, R. Fasching and F. Prinz, *Nano Lett.*, 2008, **8**, 2289–2292.
14 H. Huang, M. Nakamura, P. Su, R. Fasching, Y. Saito and F. B. Prinz, *J. Electrochem. Soc.*, 2007, **154**, B20–B24.
15 C.-W. Kwon, J.-I. Lee, K. B. Kim, H.-W. Lee, J.-H. Lee and J.-W. Son, *J. Power Sources*, 2012, **210**, 178–183.
16 A. C. Johnson, A. Baclig, D. V. Harburg, B. Lai and S. Ramanathan, *J. Power Sources*, 2010, **195**, 1149–1155.
17 D. Beckel, A. Bieberle-Hütter, A. Harvey, A. Infortuna, U. P. Muecke, M. Prestat, J. L. M. Rupp and L. J. Gauckler, *J. Power Sources*, 2007, **173**, 325–345.
18 J. Fleig, F. S. Baumann, V. Brichzin, H. R. Kim, J. Jamnik, G. Cristiani, H. U. Habermeier and J. Maier, *Fuel Cells*, 2006, **6**, 284–292.
19 J. Fleig, H. L. Tuller and J. Maier, *Solid State Ionics*, 2004, **174**, 261–270.
20 S. Litzelmann, J. Hertz and H. L. Tuller, *Fuel Cells*, 2008, **8**, 294–302.
21 A. Evans, A. Bieberle-Hütter, H. Galinski, J. L. M. Rupp, T. Ryll, B. Scherrer, R. Tölke and L. J. Gauckler, *Monatsh. Chem.*, 2009, **140**, 975–983.
22 J. H. Shim, C. Chao, H. Huang and F. B. Prinz, *Chem. Mater.*, 2007, **15**, 3850–3854.
23 P. Plonczak, A. Bieberle-Hütter, M. Sogaard, J. Martynczuk, P. Vang Hendriksen and L. J. Gauckler, *Adv. Funct. Mater.*, 2011, **21**, 2764–2775.
24 P. Plonczak, M. Sogaard, A. Bieberle-Hütter, P. Vang Hendriksen and L. J. Gauckler, *J. Electrochem. Soc.*, 2012, **159**, B1–B12.
25 T. Ryll, H. Galinski, L. Schlagenhauf, A. Bieberle-Hutter, L. J. M. Rupp and L. J. Gauckler, *Adv. Funct. Mater.*, 2011, **21**, 565–572.
26 B. Scherrer, J. Martynczuk, H. Galinski, J. G. Grolig, S. Binder, A. Bieberle-Hütter, J. L. M. Rupp, M. Prestat and J. L. Gauckler, *Adv. Funct. Mater.*, 2012, **22**, 3509–3518.
27 B. Scherrer, S. Heiroth, A. Bieberle-Hütter, J. L. M. Rupp and L. J. Gauckler, *Adv. Funct. Mater.*, 2011, **21**, 3967–3975.
28 B. Scherrer, A. Rossi, J. Martynczuk, M. Rossell, A. Bieberle-Hütter, J. L. M. Rupp and L. J. Gauckler, *J. Power Sources*, 2011, **196**, 7372–7382.
29 A. Bieberle-Hütter, P. Reinhard, L. J. M. Rupp and L. J. Gauckler, *J. Power Sources*, 2011, **196**, 6070–6078.
30 H. S. Noh, J. -W. Son, H. Lee, J.-S. Park, H.-W. Lee and J. H. Lee, *Fuel Cells*, 2010, **10**, 1057–1065.
31 A. Tarancon, M. Burriel, J. Santiso, S. J. Skinner and J. A. Kilner, *J. Mater. Chem.*, 2010, **20**, 3799–3813.
32 J. Santiso and M. Burriel, *J. Solid State Electrochem.*, 2011, **15**, 985–1006.
33 M. V. F. Schlupp, M. Prestat, J. Martynczuk, J. L. M. Rupp, A. Bieberle-Hütter and L. J. Gauckler, *J. Power Sources*, 2012, **202**, 47–55.
34 B.-K. Lai, A. C. Johnson, H. Xiong and S. Ramanathan, *J. Power Sources*, 2009, **186**, 115–122.
35 J. H. Shim, C.-C. Chao, H. Huang and F. B. Prinz, *Chem. Mater.*, 2007, **19**, 3850–3854.
36 A. Evans, A. Bieberle-Hütter, L. J. Bonderer, S. Stuckenholz and L. J. Gauckler, *J. Power Sources*, 2011, **196**, 10069–10073.
37 C. Meier, T. Hocker, A. Bieberle-Hütter and L. J. Gauckler, *Int. J. Hydrogen Energy*, 2012, **37**, 10318–10327.
38 N. Hotz, N. Koc, T. Schwamb, N. C. Schirmer and D. Poulikakos, *AIChE J.*, 2009, **55**, 1849–1859.
39 M. J. Stutz, N. Hotz and D. Poulikakos, *Chem. Eng. Sci.*, 2006, **61**, 4027–4040.
40 A. Santis-Alvarez, M. Nabavi, N. Hild, D. Poulikakos and W. J. Stark, *Energy Environ. Sci.*, 2011, **4**, 3041–3050.
41 M. J. Stutz and D. Poulikakos, *Chem. Eng. Sci.*, 2005, **60**, 6983–6997.
42 M. J. Stutz and D. Poulikakos, *Chem. Eng. Sci.*, 2008, **63**, 1761–1770.
43 A. J. Santis-Alvarez, M. Nabavi, B. Jiang, P. Muralt and D. Poulikakos, *Chem. Eng. Sci.*, 2012, DOI: 10.1016/j.ces.2012.09.003.
44 N. Raberger, M. J. Stutz, N. Hotz and D. Poulikakos, *J. Fuel Cell Sci. Technol.*, 2009, **6**, 041001–041011.
45 A. K. Chaniotis and D. Poulikakos, *J. Power Sources*, 2005, **142**, 184–193.
46 B. Jiang, P. Muralt, P. Heeb, A. Santis-Alvarez, M. Nabavi, D. Poulikakos, P. Niedermann and T. Maeder, *Sens. Actuators, B*, 2012, in press.
47 K.-R. Hwang, C. B. Lee, S.-K. Ryi and J.-S. Park, *Int. J. Hydrogen Energy*, 2011, **36**, 473–481.
48 S. K. Ryi, J. S. Park, S. H. Cho and S. H. Kim, *J. Power Sources*, 2006, **161**, 1234–1240.
49 S. K. Ryi, J. S. Park, S. H. Choi, S. H. Cho and S. H. Kim, *Chem. Eng. J.*, 2005, **113**, 47–53.

50 W. Cai, F. Wang, A. Veen, C. Descorme, Y. Schuurman, W. Shen and C. Mirodatos, *Int. J. Hydrogen Energy*, 2010, **35**, 1152–1159.
51 Y. Men, G. Kolb, R. Zapf, V. Hessel and H. Lowe, *Process Saf. Environ. Prot.*, 2007, **85**, 413–418.
52 J. W. Ha, J. H. Jang, J. H. Gil and S.-H. Kim, *Int. J. Hydrogen Energy*, 2008, **33**, 2059–2063.
53 J. D. Holladay, E. O. Jones, R. A. Dagle, G. G. Xia, C. Cao and Y. Wang, *J. Power Sources*, 2004, **131**, 69–72.
54 J.-Y. Jang, Y.-X. Huang and C.-H. Cheng, *Chem. Eng. Sci.*, 2010, **65**, 5495–5406.
55 J. Jin and S. Kwon, *Int. J. Hydrogen Energy*, 2010, **35**, 1803–1811.
56 Y. Kawamura, N. Ogura, T. Yamamoto and A. Igarashi, *Chem. Eng. Sci.*, 2006, 61.
57 T. Kim, J. S. Hwang and S. Kwon, *Lab Chip*, 2007, **7**, 835–841.
58 T. Kim and S. Kwon, *Sens. Actuators, A*, 2009, **A 154**, 204–211.
59 T. Kim, *Int. J. Hydrogen Energy*, 2009, **34**, 6790–6798.
60 A. Kundu, J. H. Jang, R. Lee, S.-H. Kim, J. H. Gil, C. R. KJung and Y. S. Oh, *J. Power Sources*, 2006, **162**, 572–578.
61 O. J. Kwon, S.-M. Hwang, J.-G. Ahn and J. J. Kim, *J. Power Sources*, 2006, **156**, 253–259.
62 A. L. Y. Tonkovich, J. L. Zilka, M. R. Powell and C. J. Call, *presented in part at the 2nd Intern. Conf. on Microreaction Technology*, New Orleans, USA, 1998.
63 K. Jähnisch, V. Hessel, H. Löwe and M. Baerns, *Angew. Chem., Int. Ed.*, 2004, **43**, 406–446.
64 L. R. Arana, S. B. Schaevitz, A. J. Franz, M. A. Schmidt and K. F. Jensen, *J. Microelectromech. Syst.*, 2003, **12**, 600–612.
65 S. Tanaka, K.-S. Chang, K.-B. Min, D. Satoh, K. Yoshida and M. Esashi, *Chem. Eng. J.*, 2004, **101**, 143–149.
66 W. J. Stark, M. Maciejewski, L. Madler, S. E. Pratsinis and A. Baiker, *J. Catal.*, 2003, **220**, 35–43.
67 G. S. Iles and R. F. Tindall, *Platinum Met. Rev.*, 1975, **19**, 42–47.
68 Z. Zhan, D. M. Bierschenk, J. S. Cronin and S. A. Barnett, *Energy Environ. Sci.*, 2011, **4**, 3951–3954.
69 R. E. Hayes and S. T. Kolaczkowski, *Introduction to Catalytic Combustion*, Taylor & Francis, 1997.